Applied Surface Science 433 (2018) 27–34

Contents lists available at ScienceDirect

Applied Surface Science

journal homepage: www.elsevier.com/locate/apsusc

Full Length Article

Influence of Nb-doped TiO_2 blocking layers as a cascading band structure for enhanced photovoltaic properties

Bon-Ryul Koo [a], Dong-Hyeun Oh [b], Hyo-Jin Ahn [a,b,*]

[a] Program of Materials Science & Engineering, Convergence Institute of Biomedical Engineering and Biomaterials, Seoul National University of Science and Technology, Seoul 01811, Republic of Korea
[b] Department of Materials Science and Engineering, Seoul National University of Science and Technology, Seoul 01811, Republic of Korea

ARTICLE INFO

Article history:
Received 7 July 2017
Received in revised form 7 September 2017
Accepted 11 October 2017
Available online 14 October 2017

Keywords:
Dye-sensitive solar cells
Nb-doped TiO_2
Blocking layers
Ultrasonic spray pyrolysis deposition
Cascading band structure

ABSTRACT

Nb-doped TiO_2 (Nb-TiO_2) blocking layers (BLs) were developed using horizontal ultrasonic spray pyrolysis deposition (HUSPD). In order to improve the photovoltaic properties of the dye-sensitized solar cells (DSSCs), we optimized the Nb doping level of the Nb-TiO_2 BLs by controlling the Nb/Ti molar ratio (0, 5, 6, and 7) of the precursor solution for HUSPD. Compared to bare TiO_2 BLs, the Nb-TiO_2 BLs formed a cascading band structure using the positive shift of the conduction band minimum of the Nb-TiO_2 positioned between fluorine-doped tin oxide (FTO) and TiO_2. This results in the increase of the potential current and the suppression of the electron recombination. Hence, it led to the improvement of the electrical conductivity, due to the increased electron concentration by the Nb doping into TiO_2. Therefore, the DSSC fabricated with the Nb-TiO_2 BLs at a Nb/Ti molar ratio of 6 showed superior photoconversion efficiency ($\sim 7.50 \pm 0.20\%$) as a result of the improved short-circuit current density. This is higher than those with the other Nb-TiO_2 BLs and without BL. This improvement of the photovoltaic properties for the DSSCs can be attributed to the synergistic effects of uniform and compact BL relative to the prevention of the backward electron transport at the FTO/electrolyte interface, efficient electron transport at interfaces relative to a cascading band structure of FTO/Nb-TiO_2/TiO_2 multilayers and the facilitated electron transport at the BLs relative to the increased electrical conductivity of the optimized Nb-TiO_2 BLs.

1. Introduction

Dye-sensitized solar cells (DSSCs) are an imperative solar energy source that has been extensively studied due to its simple structure, low manufacturing costs, and high energy conversion efficiency [1–3]. In general, DSSCs consist of transparent conducting electrodes (TCEs) based on fluorine-doped tin oxide (FTO), counter electrodes based on Pt catalysts, working electrodes based on a TiO_2 semiconductor adsorbed by Ru dye, and an electrolyte based on iodide/triiodide (I^-/I_3^-) redox couples [4]. The main factor for the DSSC operation is the behavior of an excited electron by a photon from the lowest unoccupied molecular orbital (LUMO) to the highest occupied molecular orbital (HOMO) in the dye. That is, this electron is injected into the conduction band of the TiO_2 and is progressively moved into the FTO and the external circuit to reach the Pt counter electrode. The I^-/I_3^- redox couple then regenerates the dye of the injected electron, resulting in the reversible drive of the DSSCs under illumination [5,6]. Therefore, to obtain meaningful electricity from the DSSCs, the photoexited electron is required to pass four important interfaces: counter electrode/electrolyte, electrolyte/dye, dye/TiO_2, and TiO_2/FTO. The efficient photon-to-electricity conversion in the DSSCs is directly related to the nanoporous nature of the TiO_2 layer in the working electrode, as it is possible to improve solar light absorption and dye loading due to the high surface area [7]. However, this nanoporous property can generate the FTO surface exposed to the electrolyte, where the photoexited electron may experience a charge recombination with I_3^- in the redox electrolyte ($2e^- + I_3^- \rightarrow 3I^-$) on the TiO_2/FTO interface. This causes a serious decrease in the photoconversion efficiency (PEC, η) of the DSSCs from the loss of the open circuit voltage (V_{OC}) and the short-circuit current density (J_{SC}) [6].

For the DSSCs, suppressing the charge recombination at the interface is a critical factor that can allow for the enhancement of the photovoltaic properties. This is achieved by introducing metal oxides (TiO_2, Nb_2O_5, ZnO, MgO, and $BaTiO_3$) as blocking layers (BLs)

* Corresponding author at: Department of Materials Science and Engineering, Seoul National University of Science and Technology, Seoul, 01811, Republic of Korea.
E-mail address: hjahn@seoultech.ac.kr (H.-J. Ahn).

https://doi.org/10.1016/j.apsusc.2017.10.078
0169-4332/

between the FTO and TiO_2. The BLs form an energy barrier and play a role in reducing the contact surface of the FTO and electrolyte [6,8–10]. In general, a compact TiO_2 layer prepared using a TiO_2 aqueous solution soaking method or an organic sol dip-coating method was applied to act as effective BLs on the FTO/TiO_2 interface to obstruct the back transport of the electron from the FTO to the electrolyte [11,12]. Although this method is inexpensive and simple, it tends to cause uneven and thick TiO_2 layers due to its unsophisticated deposition process. This may result in the depressed PCE of the DSSCs due to the blocked pathways of the photoexcited electrons from the TiO_2 to the FTO. Recently, much effort has been invested to develop high-performance DSSC BLs using the sputtering method, the pulsed laser deposition method, and the atomic layer deposition method [5,13,14]. While it is useful to fabricate high-quality film nanostructures with superb step coverage using these methods, there are many drawbacks, such as a high vacuum environment ($<10^{-4}$ Pa), the use of sophisticated equipment and complicated fabrication procedures, and limiting the large-scale and low-cost deposition for commercialization [15,16]. An alternative straightforward method is the horizontal ultrasonic spray pyrolysis deposition (HUSPD) method. This constructs the film nanostructure through precursor droplets formed using ultrasonic atomization, a cost-effective deposition method [17–19]. This method has the attractive advantage of fabricating uniform film structures with a high step coverage due to the uniform supply of the precursor droplets by a horizontal gas flow. However, the fabrication of uniform BLs using HUSPD has not yet been investigated. In particular, the development of novel strategies to obtain high-performance BLs is a challenging subject for the performance improvement of DSSCs. Thus, in the present study, we introduced Nb-doped TiO_2 (Nb-TiO_2) BLs for the DSSCs using HUSPD. The Nb-TiO_2 can be considered as an attractive BL due to its unique characteristics of superb electrical conductivity and optical transmittance as compared to the conventional TiO_2 BLs [20]. In addition, the correlation between photovoltaic properties and the Nb-TiO_2 BLs on the DSSCs have been investigated by adjusting the Nb/Ti molar ratio of the precursor solution during the HUSPD.

2. Experiments

2.1. Preparation of Nb-TiO_2 BLs

The Nb-TiO_2 BLs were prepared using HUSPD (Solarceramic, Nano SPD, TV500, Korea) on FTO glass (Pilkington, 8 Ω/□). For this, titanium diisopropoxide ($C_{16}H_{28}O_6Ti$, Alfa Aesar) and niobium chloride ($NbCl_5$, Aldrich) were dissolved in 50 ml ethyl alcohol (C_2H_5OH, Duksan), whereby the molar concentration of the titanium precursor was 0.5 M and the mole ratios of Nb/Ti varied between 0, 5, 6, and 7 to optimize the photovoltaic properties for the DSCCs. After stirring for 1 h, the resultant precursor solutions were sprayed using the ultrasonic atomizer (1.6 MHz) onto the FTO glass positioned in a reaction chamber at 400 °C. The air used as a carrier gas flowed with the speed of 15 l/min and the spraying time was fixed at 20 min. The samples were then allowed to cool naturally in the reaction chamber, resulting in the formation of the Nb-TiO_2 BLs with four different mole ratios of Nb/Ti (0, 5, 6, and 7) using the HUSPD, denoted as bare TiO_2, 5Nb-TiO_2, 6Nb-TiO_2, and 7Nb-TiO_2, respectively.

2.2. Fabrication of DSSCs

To prepare working electrodes, TiO_2 pastes containing 0.65 g P25 (DEGUSSA), 0.47 g hydrozypropyl cellulose (HPC, M_W = 80,000 g/mol, Aldrich), and 0.26 ml acetyl acetone ($C_5H_8O_2$, Aldrich) dissolved in 1.5 ml deionized water were coated via the squeeze-printing method (adhesive tape with approximately 16.0 um in thickness was used as spacer) onto the FTO glasses introduced with the Nb-TiO_2 BLs, and annealed at 500 °C for 1 h. The adsorption of the dye onto the TiO_2 surface was then performed by soaking the resultant electrodes in a N719 dye solution with 0.5 mM $Ru(dcbpy)_2(NCS)_2$ (N719, Ruthenizer 535-bis TBA, Solaronix) and ethanol (C_2H_6O, Aldrich) for 24 h, at room temperature. The counter electrodes were prepared on the FTO glasses by spin-coting a 5 mM platinum solution prepared with chloroplatinic acid hydrate ($H_2PtCl{\cdot}xH_2O$, Aldrich) and 2-propanol ($(CH_3)_2CHOH$, Aldrich) and then annealed at 450 °C for 30 min to form thin Pt films. Sandwich-type DSSCs were then assembled by clipping the working electrodes and counter electrodes and filling a 0.6 M BMII (1-Butyl-3-methylimidazolium iodide)-based iodine electrolyte between the electrodes.

2.3. Characterization

The surface morphology was examined by field-emission scanning electron microscopy (FESEM, Hitachi S-4800). The crystal structure and chemical bonding states were characterized by X-ray diffraction (XRD, Rigaku Rint 2500) and X-ray photoelectron spectroscopy (XPS, ESCALAB 250), respectively. Their electrical and optical properties were measured by a Hall-effect measurement system (Ecopia, HMS-3000) and ultraviolet-visible (UV-vis) spectroscopy (Perkim-Elmer, Lambda-35), respectively. The open-circuit photovoltage decay (OCVD) measurements were carried out using a poteniostat/galvanostat (PGST302N, Eco chemie). The DSSCs were illuminated for several seconds during the OCVD measurements. The photocurrent (J)–voltage (V) characteristics of the DSSCs were analyzed by solar simulator (HS technologies, PEC-L01, 150 W Xenon Arc Lamp) under standard irradiation (AM 1.5 simulated sunlight), with the intensity of 100 mW/cm^2. Electrochemical impedance spectroscopy (EIS) measurements were performed using a poteniostat/galvanostat under illumination and by employing the amplitude of 10 mV over the frequency range of 100 kHz–0.1 Hz.

3. Results and discussion

Fig. 1(a–e) present top-view FESEM images obtained from only FTO glass, bare TiO_2, 5Nb-TiO_2, 6Nb-TiO_2, and 7Nb-TiO_2, respectively, to investigate surface morphologies. The only FTO glass has a surface morphology of pyramidal crystal grains with smooth crystal faces as connections (Fig. 1(a)). After the HUSPD, the samples shown in Fig. 1(b–e) reveal that nanoparticles with 34.2–46.0 nm in diameter are compactly covered on the FTO morphology. In addition, in the cross-view FESEM images (Fig. S1), a clear observation of a thin layer with a high step coverage (68.0–79.2 nm in thickness) is equally confirmed to be present on the samples prepared by the varied Nb/Ti mole ratios. Therefore, this indicates that the FTO glass was uniformly covered with a compact Nb-TiO_2 layer, without a change of morphology and thickness and with an increase of the Nb/Ti molar ratio. This can act as a BL between the FTO used as a transparent conducting electrode and electrolyte for suppressing electron recombination in the DSSCs [21].

To investigate the crystal structure of the Nb-TiO_2 BLs with the different Nb/Ti molar ratios, we carried out the XRD analysis using the samples formed on bare glass (Corning EAGLE XG™). As shown in Fig. 2(a), all samples show clear diffraction peaks at ~25.3°, which corresponds to the (101) plane of the anatase TiO_2 phase (JCPDS card no.841286, $I4_1/amd$ [141]). From this peak, the gradual shift towards low angles was detected by increasing the Nb/Ti molar ratio (see Fig. 2(b)). This means that Nb^{5+} (0.64 Å) with a larger ionic radius than that of Ti^{4+} (0.61 Å) was incorporated into TiO_2

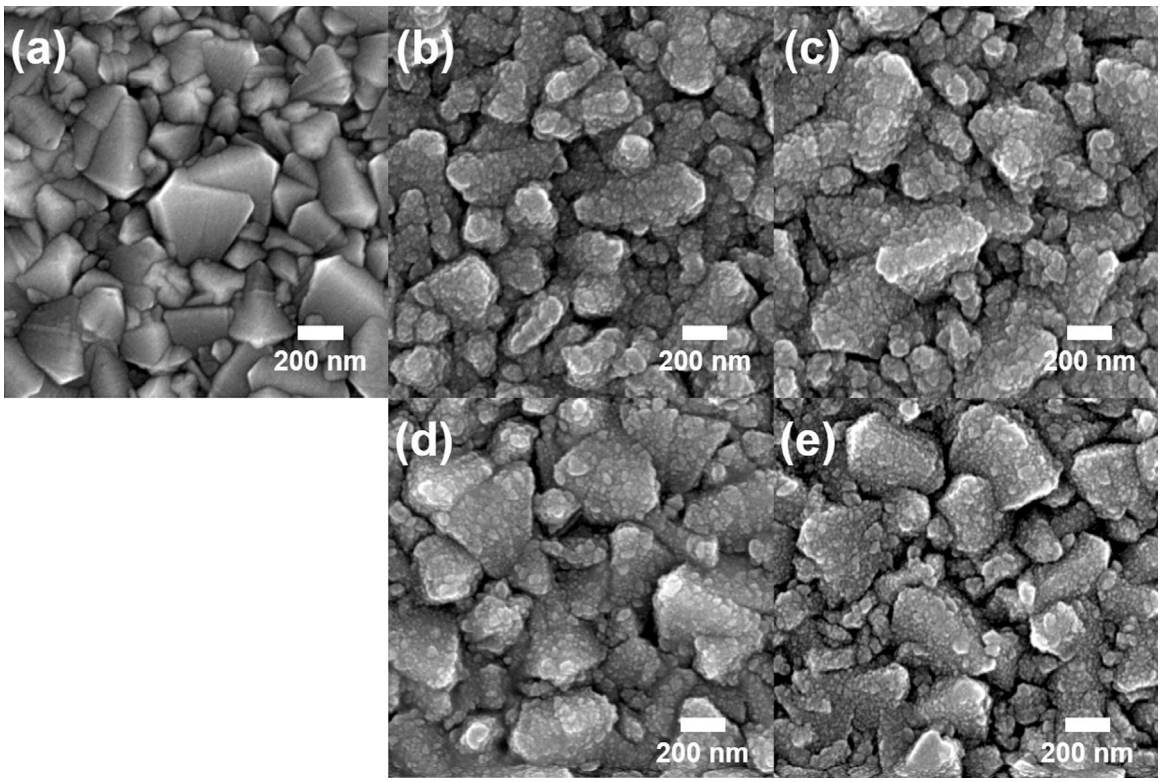

Fig. 1. Top-view FESEM images of (a) only FTO glass, (b) bare TiO_2, (c) 5Nb-TiO_2, (d) 6Nb-TiO_2, and (e) 7Nb-TiO_2.

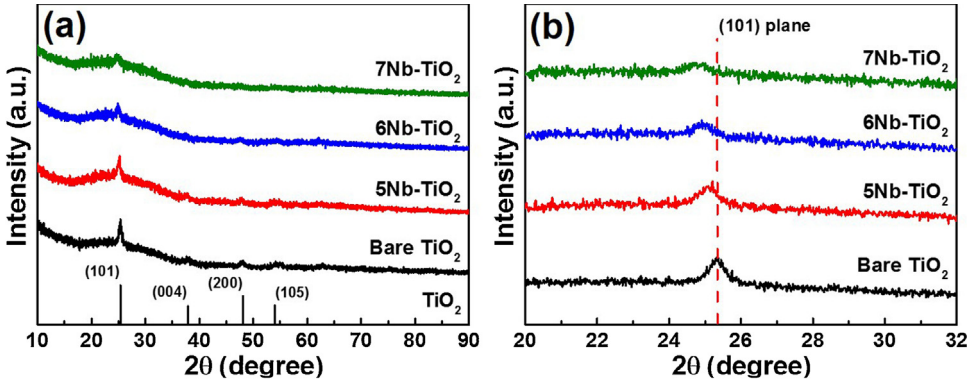

Fig. 2. (a) XRD pattern of bare TiO_2, 5Nb-TiO_2, 6Nb-TiO_2, and 7Nb-TiO_2. (b) the detailed XRD pattern of the (101) peak.

lattices, defined by the Bragg equation ($2d\sin\theta = \lambda$) [22,23]. In addition, the intensity of the (101) plane was gradually reduced with the increase of the Nb/Ti molar ratio, indicating the deterioration of the crystalline quality of the samples. This could probably be attributed to the lattice distortion caused by the difference in the ionic radius between Nb^{5+} and Ti^{4+} [24], which is confirmed by the increased lattice parameters *a* and *c* of the samples (see Fig. S2). This deterioration of crystalline quality can lead to the decline of electron mobility resulting from the grain boundary scattering, which may affect current density relative to the photovoltaic properties for the DSSCs [25]. Therefore, the XRD results indicate the successful formation of the Nb-TiO_2 BLs, with the adjustable Nb/Ti molar ratio using the HUSPD.

Fig. 3 shows XPS core-level spectra of Ti 2*p* and Nb 3*d* for all samples, used to derive the surface chemical binding states. All binding energies were corrected using the C 1*s* of 284.5 eV as reference. For the Ti 2*p* XPS core-level spectra of bare TiO_2 shown in Fig. 3(a), a dominant peak was emitted at 458.3 eV for Ti $2p_{3/2}$ and 464.0 eV for Ti $2p_{1/2}$, which corresponds to the Ti^{4+} oxidation state relative to the TiO_2 phase [26]. On the other hand, the samples of the Nb-TiO_2 BLs (see Fig. 3(b–d)) also exhibit a major peak at 458.4 eV for Ti $2p_{3/2}$ and 464.1 eV for Ti $2p_{1/2}$, as well as a minor peak at 456.8 eV for Ti $2p_{3/2}$ and 462.7 eV for Ti $2p_{1/2}$, indicating the Ti^{4+} and Ti^{3+} oxidation states, respectively [27,28]. In addition, from the Nb 3*d* XPS core-level spectra (see Fig. 3(e–g)), a pronounced peak at 207.0 eV is revealed for Nb $3d_{5/2}$ and 209.8 eV for Nb $3d_{3/2}$, and a weak peak at 205.9 eV for Nb $3d_{5/2}$ and 209.1 eV for Nb $3d_{3/2}$, which can be assigned as the Nb^{5+} and Nb^{4+} oxidation states, respectively. This existence of Ti^{4+} and Nb^{5+} is evidence that the Nb atom is doped into TiO_2 lattices. According to the results of Lei et al. and Potlog et al., the doped Nb atom leads to the formation of one delocalized electron, which can fill the state near the bottom of the conduction band induced from Ti3*d* and Nb3*d* orbitals, as predicted by the existence of minor Ti^{3+} and Nb^{4+} oxidation states [27,28]. In particular, the remarkable difference in the peak area ratio of the Nb 3*d*/Ti 2*p* photoelectrons is observed with the increasing Nb/Ti molar ratio

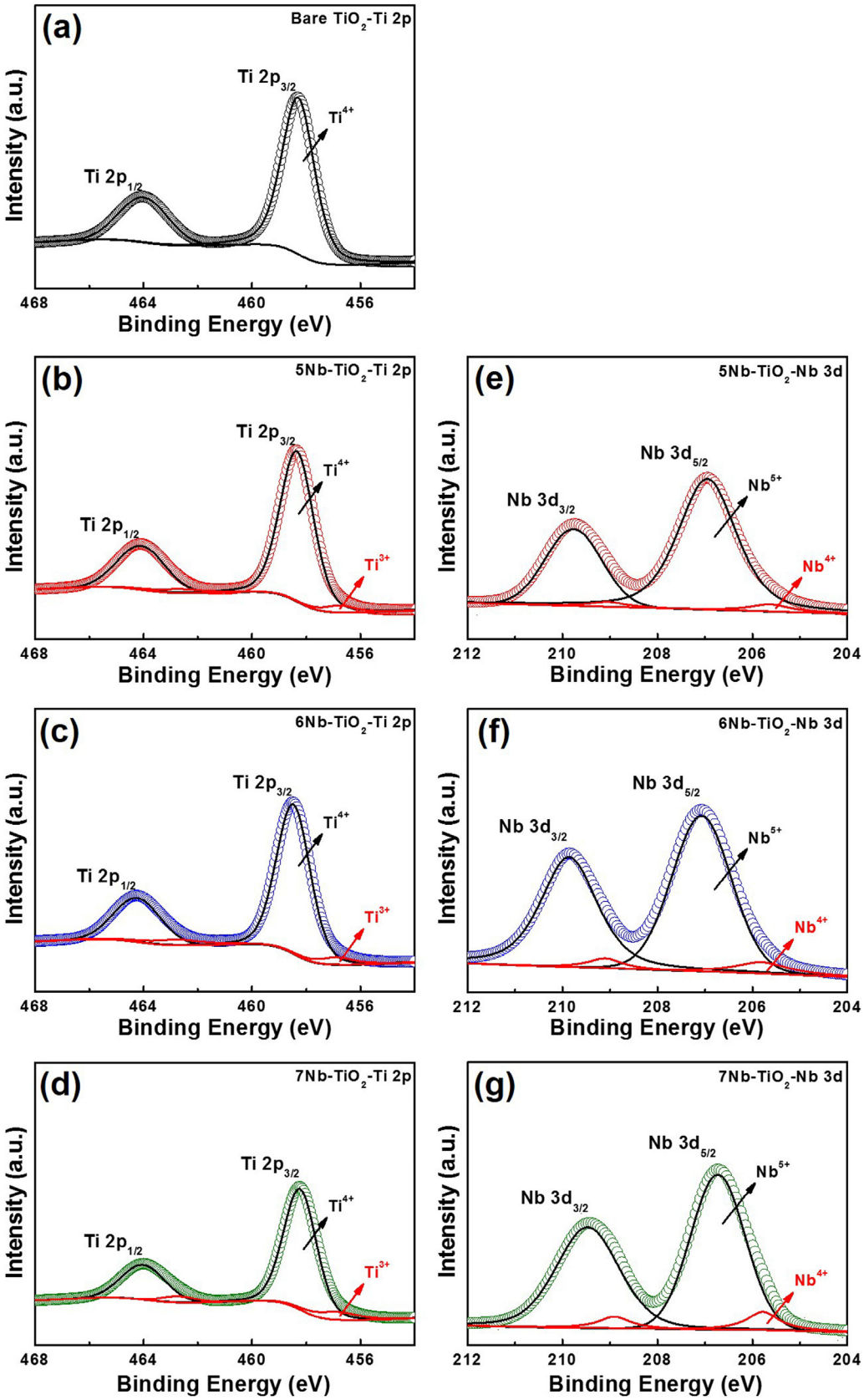

Fig. 3. XPS core-level spectra of (a) Ti 2*p* obtained from bare TiO_2 and (b-d) Ti 2*p* and (e-g) Nb 3*d* obtained from 5Nb-TiO_2, 6Nb-TiO_2, and 7Nb-TiO_2.

of the precursor solution for fabricating the Nb-TiO_2 BLs. Therefore, to determine their Nb-doping level, we calculated the atomic percentage of the Ti, O, and Nb elements, using the peak areas of the XPS core-level spectra. As shown in Table S1, as the Nb/Ti molar ratio of the precursor solution for HUSPD increases, the ratios of the Nb/Ti atomic percentage (2.42 for 5Nb-TiO_2, 2.71 for 6Nb-TiO_2, and

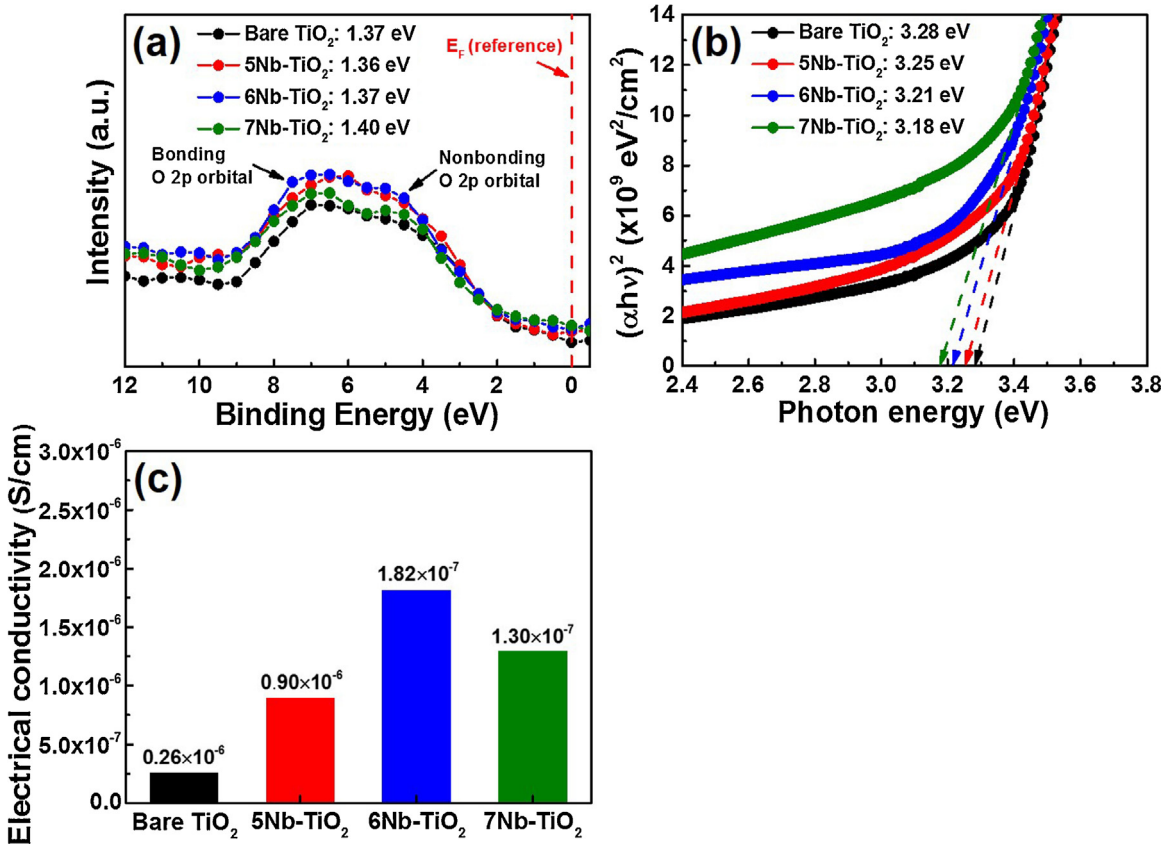

Fig. 4. (a) Valence band XPS spectra, (b) plots of $(ahv)^2$ versus photon energy, and (c) electrical conductivity of the Nb-TiO_2 BLs with Nb/Ti molar ratio of 0, 5, 6, and 7.

3.03 for 7Nb-TiO_2) are enhanced. This result can raise the electron concentration affecting optical and electrical properties of the BLs for the DSSCs ($Nb_2O_5 \rightarrow 2Nb_{Ti}^{\cdot} + 4O_O^{\times} + 1/2O_2(g) + 2e^-$) [29,30].

To trace the relative position of the conduction band minimum (CBM) onto the Nb-TiO_2 BLs with the varied Nb/Ti molar ratio related to photovoltaic properties for the DSSCs, the analysis of the valence-band XPS spectrum was performed (see Fig. 4(a)). In valence band XPS spectra, the two arrows (black) are attributed to the electron emission from nonbonding (π) and bonding (σ) O 2*p* orbitals, respectively. In addition, because the binding energy of this spectra is referenced to Fermi level, the bonding energy of 0 eV (red line) corresponds to Fermi level. In addition, the position of the valence band maximum (VBM) is determined by means of a linear extrapolation of the onset of the valence band emission [31]. The VBM appears to be located at a similar position among the samples. Based on these considerations, we deduced that the relative position of the CBM is determined by the optical bandgap (E_g). Fig. 4(b) shows the plot of $(\alpha h\nu)^2$ versus photon energy ($h\nu$) obtained from the transmittance spectra of the samples, in which the optical bandgap can be calculated by the following equation (see Eq. (1)) [32]:

$$\alpha h\nu = A(h\nu - E_g)^n \quad (1)$$

where α is the optical absorption coefficient, A is an energy-independent constant, and n is constant. The calculated values of the optical bandgap are decreased from 3.28 eV for bare TiO_2 to 3.18 eV for 7Nb-TiO_2, as an effect of the increased Nb doping. This is attributed to the increase in the electron concentration near the bottom of the conduction band[30]. With an estimated VBM and optical bandgap, it can be predicted that the increase of Nb doping into the TiO_2 lattices leads to a gradual positive shift of the CBM (see Table S2 for a summary). This can cause the formation of a cascading band structure with the introduction of the Nb-TiO_2 BLs between the FTO and TiO_2. This is useful in increasing the potential current relative to the electron transport and minimizing the electron recombination at the interfaces [33]. In addition, the electrical conductivity (see Fig. 4(c)) is increased by increasing the Nb/Ti molar ratio of the Nb-TiO_2 BLs due to the higher electron concentration. This facilitates the efficient electron transport at the BLs by the introduction of the optimized Nb-TiO_2 [34]. It is well known that the high electron concentration in films can lead to the degradation in optical transmittance due to light scattering. Hence, the gradual decrease in the optical transmittance was observed with the increase of the Nb/Ti molar ratio on the Nb-TiO_2 BLs (see Fig. S3). However, 7Nb-TiO_2 has the reduced electrical conductivity compared to 6Nb-TiO_2 due to a decline of electron mobility by the deterioration of their crystalline quality. This is consistent with the previous report of Furubayashi et al. [20]. Therefore, the effect of the formed cascading band structure and increased electrical conductivity by the Nb-TiO_2 BLs can cause the improvement of the photovoltaic properties for the DSSCs [9,30].

Fig. 5(a) shows the OCVD curve of the DSSCs with the Nb-TiO_2 BLs and without BL, whereby OCVD is an important technique to monitor the subsequent decay of the V_{OC} after stopping the illumination in a steady state [35]. The decay of the V_{OC} indicates the decrease of electron concentration at the FTO, caused by the electron recombination. It is obvious that the OCVD response of the DSSCs with the Nb-TiO_2 BLs was much slower than the one without the BL, which can be attributed to the suppressed electron recombination by the introduction of the BL. This subsequently results in higher photovoltaic properties due to more electrons accumulated from the electrolyte to the FTO in the DSSCs [21]. In addition, with the increase of the Nb/Ti molar ratio on the Nb-TiO_2 BLs, the OCVD response gradually slowed down and then sped up when the

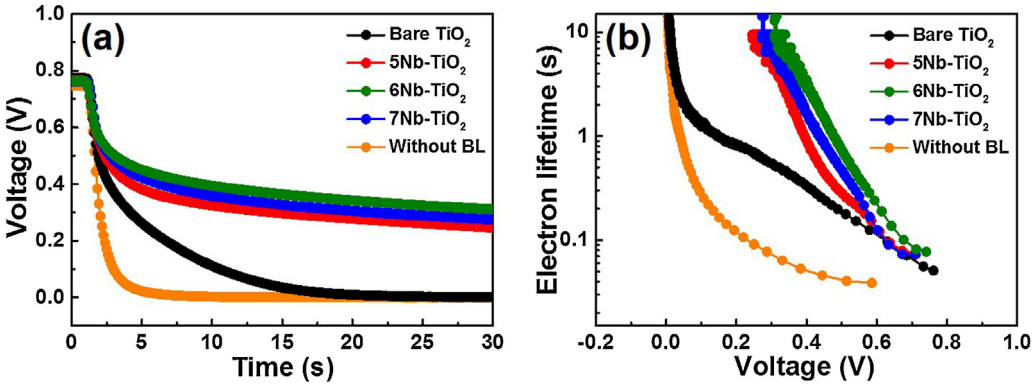

Fig. 5. (a) OCVD curve of the DSSCs with bare TiO_2, 5Nb-TiO_2, 6Nb-TiO_2, and 7Nb-TiO_2 and without the BLs. (b) Comparison of electron lifetime among the samples as a function of voltage.

Nb/Ti molar ratio reached 7. This result is related to the formation of a cascading band structure and increased electrical conductivity due to the effect of the Nb doping into the TiO_2 lattices. In order to quantify the extent of the electron recombination between the electrolyte and the FTO, we compared the electron lifetime (τ_n) calculated with the OCVD results, which is derived from the following equation (see Eq. (2)) [35]:

$$\tau_{n=} -(k_B T/e)(dV_{OC}/dt)^{-1} \quad (2)$$

where $k_B T$ is the thermal energy, e is the positive elementary charge, and dV_{OC}/dt is the derivative of the transient open-circuit voltage. The calculated electron lifetime at 0.4 V is 0.71 s for bare TiO_2, 1.21 s for 5Nb-TiO_2, 4.06 s for 6Nb-TiO_2, and 2.14 s for 7Nb-TiO_2, which is higher than that without the BLs (0.05 s). In particular, this result provides the clear evidence that 6Nb-TiO_2 exhibits the longest electron lifetime compared to the other samples, meaning that the electrons can survive longer and transport with a smaller loss on the FTO/electrolyte interface [35]. This can be attributed to the decreased interfacial resistance at the working electrode, primarily due to efficient electron transport and suppressed electron recombination at the interfaces, resulting from the formation of a cascading band structure by the Nb-TiO_2 BLs (see Fig. S4). Therefore, a greater transport efficiency of the excited electrons from the electrolyte to the FTO may give rise to a short-circuit current density (J_{SC}) value relative to the photovoltaic properties for the DSSCs [34].

Fig. 6 displays the J–V curves of the DSSCs fabricated with the Nb-TiO_2 BLs and without BL. The detail photovoltaic properties obtained from the J–V curves for all samples are summarized in Table 1, in which the PCE of the DSSCs is calculated as follows (see Eq. (3)) [36]:

$$\eta(\%) = (J_{SC} \times V_{OC} \times FF)/(P_{in}) \quad (3)$$

where FF and P_{in} are the fill factor and the intensity of the incident light, respectively. Compared to the DSSC without the BLs, those with the Nb-TiO_2 BLs exhibit a pronounced increase in the V_{OC} and J_{SC} value due to the suppressed electron recombination process. Furthermore, with the increase of the Nb/Ti molar ratio on the Nb-TiO_2 BLs, while the V_{OC} value is gradually decreased by the

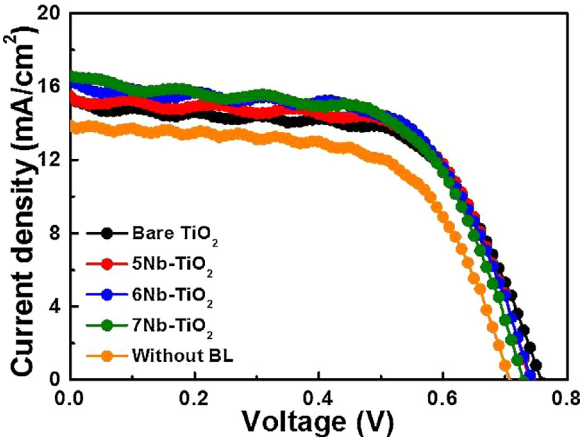

Fig. 6. (a) J–V curves of the DSSCs with the Nb-TiO_2 BLs prepared by the varied Nb/Ti molar ratios and without BL.

narrowing optical bandgap originating from the positive shift of the CBM on the Nb-TiO_2 BLs, the J_{SC} value enhances from bare TiO_2 to 6Nb-TiO_2 and decreases slightly for 7Nb-TiO_2. As a result, the DSSCs with 6Nb-TiO_2 exhibit a superior PCE (~7.50 ± 0.20%) compared to that of the other samples (~7.16 ± 0.20% for bare TiO_2, ~7.27 ± 0.27% for 5Nb-TiO_2, and ~7.29 ± 0.33% for 7Nb-TiO_2). The performance improvement is mainly attributed to the increased J_{SC} values, which are due to the synergistic effect of three factors of the Nb-TiO_2 BL on the DSSCs (see Fig. 7): (1) The uniform and compact structure of the Nb-TiO_2 layer formed by the HUSPD serves as an efficient BL to prevent backward electron transfer at the FTO/electrolyte interface. (2) A cascading band structure of the FTO/Nb-TiO_2/TiO_2 multilayers caused by the positively shifted CBM of the Nb-TiO_2 BLs can lead to the efficient electron transport at the interfaces by increasing the potential current and suppressing electron recombination. (3) The increased electrical conductivity of the Nb-TiO_2 BLs by the optimized Nb/Ti molar ratio can facilitate the electron transport at the BLs of the DSSCs. These effects of the Nb-TiO_2 BLs were also confirmed by the suppressed dark current and the shifted onset bias shown in the dark current-voltage curves (see

Table 1
Photovoltaic properties and the fitted EIS parameters of DSSCs assembled with the varied Nb-TiO_2 BLs and without the BL.

Samples	V_{OC} (V)	J_{SC} (mA/cm$_2$)	FF (%)	η (%)	R_S (Ω)	R_1 (Ω)	R_2 (Ω)	R_3 (Ω)
Bare TiO_2	0.76 ± 0.01	15.11 ± 0.50	61.05 ± 0.01	7.16 ± 0.20	18.0	8.52	22.3	5.54
5Nb-TiO_2	0.74 ± 0.01	16.28 ± 0.53	60.54 ± 0.02	7.27 ± 0.30	18.0	8.38	21.3	5.57
6Nb-TiO_2	0.74 ± 0.01	16.90 ± 0.55	60.26 ± 0.01	7.50 ± 0.20	17.8	8.44	16.3	4.91
7Nb-TiO_2	0.73 ± 0.01	16.58 ± 0.47	60.63 ± 0.05	7.29 ± 0.33	17.9	8.32	19.3	4.95
Without BL	0.71 ± 0.01	14.02 ± 0.55	61.58 ± 0.04	6.13 ± 0.22	–	–	–	–

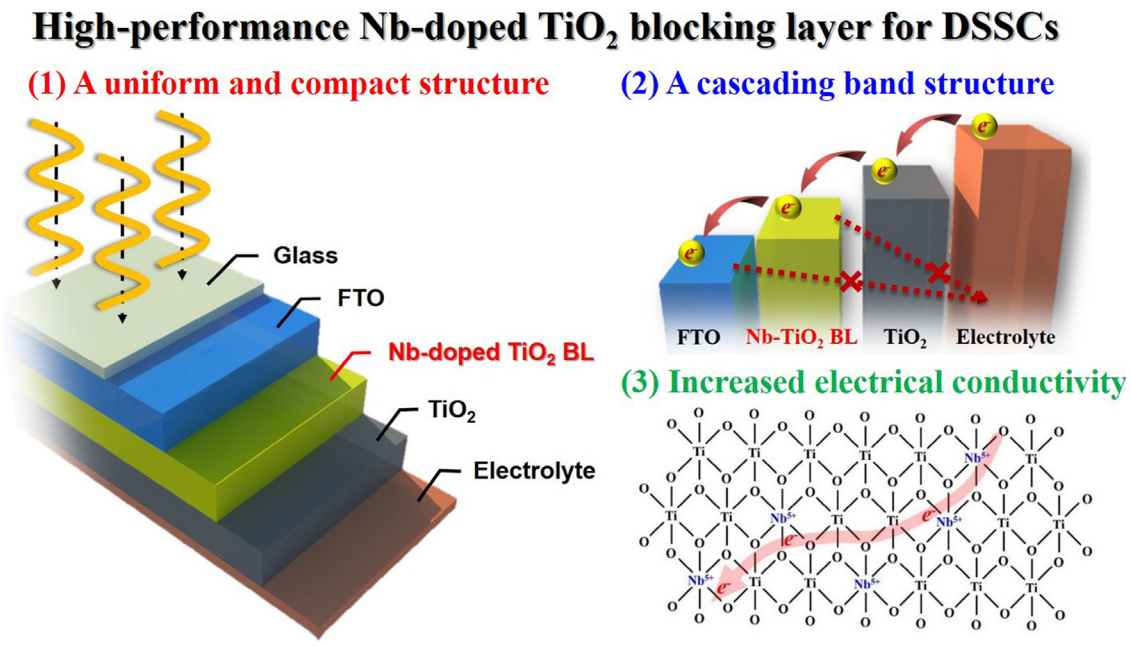

Fig. 7. Schematic of two main effects for high-performance DSSCs in the Nb-TiO_2 BLs.

Fig. S5). Therefore, we believe that the Nb-TiO_2 BLs prepared using the HUSPD play an important role in improving the photovoltaic properties of the DSSCs.

4. Conclusions

We developed the high-performance Nb-TiO_2 BLs for the DSSCs using the HUSPD by controlling the Nb/Ti molar ratio (0, 5, 6, and 7). It is noted that the effect of the Nb doping into TiO_2 has the advantage of forming a cascading band structure of the FTO/Nb-TiO_2/TiO_2 multilayers by a gradual positive shift of their CBM and increasing the electrical conductivity. As a result, when the Nb/Ti molar ratio of the Nb-TiO_2 BLs was set at 6, the DSSCs achieved an enhanced PCE ($\sim 7.50 \pm 0.20\%$) as compared to the other Nb-TiO_2 BLs and without BL. This is a result of the increased J_{SC} value from the combined effect of the three factors on the Nb-TiO_2 BLs: the uniform and compact BL formed by the HUSPD to prevent the back electron transport from the FTO and to the electrolyte, the efficient electron transport at the interfaces by a cascading band structure of FTO/Nb-TiO_2/TiO_2 multilayers to increase the potential current and suppress electron recombination, and the facilitated electron transport at the BLs resulting from increased electrical conductivity of the optimized Nb-TiO_2 BLs. Therefore, we believe that the Nb-TiO_2 layer fabricated using HUSPD has a strong potential to be used as novel BLs for the performance improvement of the DSSCs.

Acknowledgements

This research was supported by Basic Science Research Program through the National Research Foundation of Korea (NRF) funded by the Ministry of Science, ICT, and Future Planning (NRF-2015R1A1A1A05001252).

References

[1] L. Jiang, L. Sun, D. Yang, J. Zhang, Y.-J. Li, K. Zou, W.-Q. Deng, Niobium-doped (001)-dominated anatase TiO_2 nanosheets as photoelectrode for efficient dye-sensitized solar cells, ACS Appl. Mater. Interfaces 9 (2017) 9576–9583.
[2] V.A. Tran, T.T. Truong, T.A.P. Phan, T.N. Nguyen, T.A. Huynh, A. Agresti, S. Pescetelli, T.K. Le, A.D. Carlo, T. Lund, S.-N. Le, P.T. Nguyen, Application of nitrogen-doped TiO_2 nano-tubes in dye-sensitized solar cells, Appl. Surf. Sci. 399 (2017) 515–522.
[3] S.K. Pathak, A. Abate, P. Ruckdeschel, B. Roose, K.C. Gödel, Y. Vaynzof, A. Santhala, S.-I. Watanabe, D.J. Hollman, N. Noel, A. Sepe, U. Wiesner, R. Friend, H.J. Snaith, U. Steiner, Performance and stability enhancement of dye-sensitized and perovskite solar cells by Al doping of TiO_2, Adv. Funct. Mater. 24 (2014) 6046–6055.
[4] B.-R. Koo, H. An, H.-J. Ahn, High-surface area co-electrospun TiO_2 nanowites fabricated using shrinkage of polyvinylpyrrolidone for improved photovoltaic performance, Ceram. Int. 42 (2016) 1666–1671.
[5] L. Li, C. Xu, Y. Zhao, S. Chen, K.J. Ziegler, Improving performance via blocking layers in dye-sensitized solar cells based on nanowire photoanodes, ACS Appl. Mater. Interfaces 7 (2015) 12824–12831.
[6] H. Yu, S. Zhang, H. Zhao, G. Will, P. Liu, An efficient and low-cost TiO_2 compact layer for performance improvement of dye-sensitized solar cells, Electrochim. Acta 54 (2009) 1319–1324.
[7] W. Song, Y. Gong, J. Tian, G. Cao, H. Zhao, C. Sun, Novel photoanode for dye-sensitized solar cells with enhanced light-harvesting and electron-collection efficiency, ACS Appl. Mater. Interfaces 8 (2016) 13418–13425.
[8] J. Xia, N. Masaki, K. Jiang, S. Yanagida, Sputtered Nb_2O_5 as a novel blocking layer at conducting glass/TiO_2 interfaces in dye-sensitized ionic liquid solar cells, J. Phys. Chem. C 111 (2007) 8092–8097.
[9] G.S. Selopal, N. Memarian, R. Milan, I. Concina, G. Sberveglieri, A. Vomiero, Effect of blocking layer to boost photoconversion efficiency in ZnO dye-sensitized solar cells, ACS Appl. Mater. Interfaces 6 (2014) 11236–11244.
[10] K.-N. Bae, S.I. Noh, H.-J. Ahn, T.-Y. Seong, Effect of MnTiO3 surface treatment on the performance of dye-sensitized solar cells, Mater. Lett. 96 (2013) 67–70.
[11] S. Ahmed, A.D. Pasquier, T. Asefa, D.P.B. Birnie, Improving microstructured TiO_2 photoanodes for dye sensitized solar cells by simple surface treatment, Adv. Energy Mater. 1 (2011) 879–887.
[12] W. Yang, F. Wan, S. Chen, C. Jiang, Hydrothermal growth and application of ZnO nanowire films with ZnO and TiO_2 buffer layers in dye-sensitized solar cells, Nanoscale Res. Lett. 4 (2009) 1486–1492.
[13] S. Suresh, G.E. Unni, C. Ni, R.S. Sreedharan, R.R. Krishnan, M. Satyanarayana, M. Shanmugam, V.P.M. Pillai, Phase modification and morphological evolution in Nb_2O_5 thin films and its influence in dye- sensitized solar cells, Appl. Surf. Sci. 419 (2017) 720–732.
[14] N. Ali, A. Hussain, R. Ahmed, M.K. Wang, C. Zhao, B.U. Haq, Y.Q. Fu, Advances in nanostructured thin film materials for solar cell applications, Renew. Sustain. Energy Rev. 59 (2016) 726–737.
[15] B.-R. Koo, J.-W. Bae, H.-J. Ahn, Low-temperature conducting performance of transparent indium tin oxide/antimony tin oxide electrodes, Ceram. Int. 43 (2017) 6124–6129.
[16] B.-R. Koo, H.-J. Ahn, Effect of hybrid nanoinks on solution-based Sn-doped In_2O_3 films under low-temperature microwave annealing, Ceram. Int. 42 (2016) 509–517.
[17] T. Fukano, T. Motohiro, Low-temperature growth of highly crystallized transparent conductive fluorine-doped tin oxide films by intermittent spray pyrolysis deposition, Sol. Energy Mater. Sol. Cells 82 (2004) 567–575.

[18] C. Jiang, W.L. Koh, M.Y. Leung, W. Hong, Y. Li, J. Zhang, Influences of alcoholic solvents on spray pyrolysis deposition of TiO_2 blocking layer films for solid-state dye-sensitized solar cells, J. Solid State Chem. 198 (2013) 197–202.
[19] G. Zhu, T. Lv, L. Pan, Z. Sun, C. Sun, All spray pyrolysis deposited CdS sensitized ZnO films for quantum dot-sensitized solar cells, J. Alloys Compd. 509 (2011) 362–365.
[20] Y. Furubayashi, T. Hitosugi, Y. Yamamoto, K. Inaba, G. Kinoda, Y. Hirose, T. Shimada, T. Hasegawa, A transparent metal: Nb-doped anatase TiO_2, Appl. Phys. Lett. 86 (2005) 252101.
[21] J. Kim, H. Choi, C. Nahm, J. Moon, C. Kim, S. Nam, D.-R. Jung, B. Park, The effect of a blocking layer on the photovoltaic performance in CdS quantum-dot-sensitized solar cells, J. Power Sources 196 (2011) 10526–10531.
[22] X. Lü, W. Yang, Z. Quan, T. Lin, L. Bai, L. Wang, F. Huang, Y. Zhao, Enhanced electron transport in Nb-doped TiO_2 nanoparticles via pressure-induced phase transitions, J. Am. Chem. Soc. 136 (2014) 419–426.
[23] H.-D. Lim, W.M. Seong, J. Kim, B. Lee, D.H. Kim, K. Kang, Nb-doped TiO_2 air-electrode for advanced Li-air batteries, J. Asian Ceram. Soc. 3 (2015) 77–81.
[24] A.G. Manohari, K.S. Kumar, C. Lou, T. Mahalingam, C. Manoharan, Buffer layer of antimony doped tin disulphide thin films for heterojunction solar cells, Mater. Lett. 155 (2015) 121–124.
[25] H. Zhang, G. Lee, C. Gong, L. Colombo, K. Cho, Grain boundary effect on electrical transport properties of graphene, J. Phys. Chem. C 118 (2014) 2338–2343.
[26] H. An, H.-J. Ahn, A change in morphology from anatase-TiO_2 nanoparticles to anatase-TiO_2 nanoflakes via electrospray, Mater. Lett. 81 (2012) 41–44.
[27] T. Potlog, P. Dumitriu, M. Dobromir, A. Manole, D. Luca, Nb-doped TiO_2 thin films for photovoltaic applications, Mater. Des. 85 (2015) 558–563.
[28] T. Hitosugi, H. Kamisaka, K. Yamashita, H. Nogawa, Y. Furubayashi, S. Nakao, N. Yamada, A. Chikamatsu, H. Kumigashira, M. Oshima, Y. Hirose, T. Shimada, T. Hasegawa, Electronic band structure of transparent conductor: Nb-doped anatase TiO_2, Appl. Phys. Express 1 (2008) 111203.
[29] H. Su, Y.-T. Huang, Y.-H. Chang, P. Zhai, N.Y. Hau, P.C.H. Cheung, W.-T. Yeh, T.-C. Wei, S.-P. Feng, The synthesis of Nb-doped TiO_2 nanoparticles for improved-performance dye sensitized solar cells, Electrochim. Acta 182 (2015) 230–237.
[30] M. Duta, L. Predoana, J.M. C.-Moreno, S. Preda, M. Anastasescu, A. Marin, I. Dascalu, P. Chesler, C. Hornoiu, M. Zaharescu, P. Osiceanu, M. Gartner, Nb-doped TiO_2 sol–gel films for CO sensing applications, Mater. Sci. Semicond. Process. 42 (2016) 397–404.
[31] T. Nikolay, L. Larina, O. Shevaleevskiy, B.T. Ahn, Electronic structure study of lightly Nb-doped TiO_2 electrode for dye-sensitized solar cells, Energy Environ. Sci. 4 (2011) 1480–1486.
[32] C. Fu, Y. Gong, Y. Wu, J. Liu, Z. Zhang, C. Li, L. Niu, Photocatalytic enhancement of TiO_2 by B and Zr co-doping and modulation of microstructure, Appl. Surf. Sci. 379 (2016) 83–90.
[33] Z. Liu, Y. Li, C. Liu, J. Ya, E. Lei, W. Zhao, D. Zhao, L. An, TiO_2 photoanode structure with gradations in V concentration for dye-sensitized solar cells, ACS Appl. Mater. Interfaces 3 (2011) 1721–1725.
[34] M.-S. Wu, Z.-Z. Ceng, C.-Y. Chen, Surface modification of porous TiO_2 electrode through pulse oxidative hydrolysis of $TiCl_3$ as an efficient light harvesting photoanode for dye-sensitized solar cells, Electrochim. Acta 191 (2016) 256–262.
[35] C.-Y. Huang, P.-H. Chen, Y.-J. Wu, H.-P. Chiang, J.-S. Hwang, P.-T. Lin, K.-Y. Lai, F.S.-S. Chien, T.-Y. Lin, Enhanced performance of ZnO-based dye-sensitized solar cells using TiO_2/graphene nanocomposite compact layer, Jpn. J. Appl. Phys. 56 (2017) 045201.
[36] L. Chu, Z. Qin, W. Liu, X. Ma, Inhibition of charge recombination for enhanced dye-sensitized solar cells and self-powered UV sensors by surface modification, Appl. Surf. Sci. 389 (2016) 802–809.